ARTICLE

How Depletion Layers Govern the Dynamic Plasmonic Response of In-Doped CdO Nanocrystals

Sofia A. Shubert-Zuleta, Victor Segui Barragan, M. Wren Berry, Robert Russum Jr., and Delia J. Milliron*

Read Online

ACCESS | Metrics & More | Article Recommendations | Supporting Information

ABSTRACT: Doped metal oxide nanocrystals exhibit a localized surface plasmon resonance that is widely tunable across the mid- to near-infrared region, making them useful for applications in optoelectronics, sensing, and photocatalysis. Surface states pin the Fermi level and induce a surface depletion layer that hinders conductivity and refractive index sensing but can be advantageous for optical modulation. Several strategies have been developed to both synthetically and postsynthetically tailor the depletion layer toward particular applications; however, this understanding has primarily been advanced in Sn-doped In_2O_3 (ITO) nanocrystals, leaving open questions about generalizing to other doped metal oxides. Here, we quantitatively analyze the depletion layer in In-doped CdO (ICO) nanocrystals, which is shown to have an intrinsically wide depletion layer that leads to broad plasmonic modulation via postsynthetic chemical reduction and ligand exchange. Leveraging these insights, we applied depletion layer tuning to enhance the inherently weak plasmonic coupling in ICO nanocrystal superlattices. Our results demonstrate how an electronic band structure dictates the radial distribution of electrons and governs the response to postsynthetic modulation, enabling the design of tunable and responsive plasmonic materials.

KEYWORDS: transparent conducting oxide, band bending, localized surface plasmon resonance, redox, ligand exchange, superlattice, space charge layer
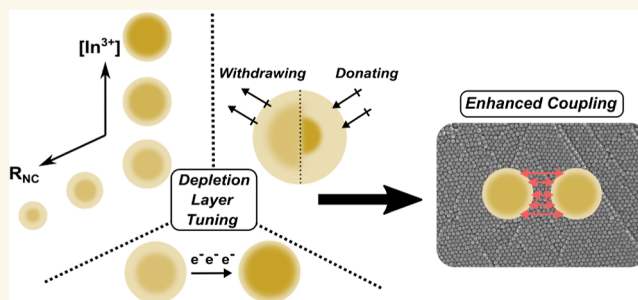
INTRODUCTION

The resonant oscillation of conduction electrons confined to nanosized volumes gives rise to localized surface plasmon resonance (LSPR) absorption at a frequency dependent on the carrier concentration in the plasmonic material. LSPR has been extensively studied in noble metals, such as Ag and Au nanocrystals (NCs); however, the electron concentration is largely a fixed, intrinsic property in conventional metals, leading to an emphasis on shape and size instead as the primary means for tuning the LSPR. Semiconductor NCs have emerged as a more adaptable class of plasmonic materials because they exhibit LSPR that varies widely across the visible to mid-infrared (IR) by tuning the doping concentration or host material composition.[1−4] Plasmonic metal oxide NCs, such as Sn-doped In_2O_3 (ITO), Al-doped ZnO (AZO), and $WO_{3−x}$, can be used to form transparent and conductive thin films that make them suitable for optoelectronic applications such as electrochromic smart windows[5,6] and photovoltaics.[7] NC surface states, commonly hydroxyl groups in metal oxides, induce Fermi level pinning of the NC to maintain overall charge neutrality, resulting in equilibration of the surface

potential with the NC Fermi level potential. Furthermore, with midgap surface states below the flat band NC Fermi level, the NC conduction and valence bands bend upward in response to equilibration and form a near-surface depletion layer.[8−10] While the depletion layer can be considered a drawback in applications that rely on inter-NC charge transfer[11] or sensitivity to the surrounding dielectric environment,[12,13] it can also be leveraged as a charge storage region that enhances the LSPR modulation range.[14−16] The effect of the depletion layer on optical and electronic properties has been extensively studied in ITO NCs[12−14,17−25] and to a much lesser extent in AZO NCs,[26] but understanding how its characteristics depend on the attributes of the host material will unlock the potential
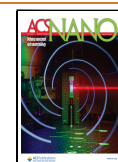
for depletion layer engineering in various applications of these emerging plasmonic nanomaterials.[16,20]

The radial depletion layer width (W_d) in spherical NCs is well approximated by Poisson's equation for the depletion layer in planar electrodes, eq 1.[27] In eq 1, ϵ_0 is the vacuum permittivity, ϵ_R is the relative dielectric constant, e is the elementary charge, N_d is the donor density, and E_{BI} is the built-in potential, which is the potential difference between the flat band Fermi level potential, $E_{F,fb}$, and the surface potential, E_S. This relationship is visually represented in Figure 1, where r_0
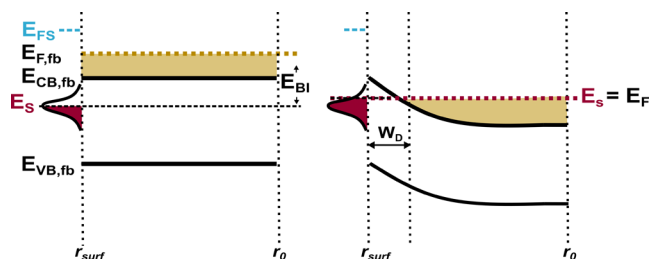

Figure 1. Schematic representation of the electronic structure under flat band conditions before equilibration with the surface state potential (left, "fb" subscripts) and equilibrated state (right) that causes band bending and depletion layer formation. r_0 and r_{surf} indicate the NC center and surface, respectively. E_{FS} is the Fermi level stabilization potential, an upper limit on increasing the E_F.[31]

and r_{surf} indicate the NC center and surface, respectively. In NCs, W_d can be tuned by changing (1) N_d via the doping concentration and (2) E_{BI} via the E_S.[8,13] Due to the different bonding motifs, facets, or identity of such surface states, there exists a potential range of surface states where E_S denotes the highest occupied electronic state that is isoenergetic with the pinned Fermi level, E_F, after equilibration of the system. Increasing the N_d via aliovalent doping during synthesis of ITO NCs is known to stabilize the band edges while maintaining E_S and consequently, narrowing W_d until it is virtually eliminated.[18,28−30] However, to enable dynamic and reversible depletion layer tuning, postsynthetic strategies, such as those that modulate E_{BI}, must be employed.

$$W_d = \sqrt{\frac{2\epsilon_R\epsilon_0 E_{BI}}{eN_d}} \qquad (1)$$

One strategy to dynamically tune E_{BI} is postsynthetic doping such as electrochemical doping,[13,23,32,33] photodoping,[16,29,34] or chemical redox doping,[14,35,36] all of which progressively raise the E_S, thus increasing the pinned E_F, reducing E_{BI}, and narrowing W_d. Upon E_F reaching the Fermi level stabilization potential (E_{FS}), added dopants are readily compensated and do not donate electrons to the NC conduction band; therefore, $E_{FS} = E_F$ represents the NC electron saturation condition.[31,37,38] The aforementioned postsynthetic doping treatments cause changes in the LSPR intensity, frequency, and line shape, all of which have been well-studied for ITO NCs. Another technique to tune W_d and thus LSPR is via a partial exchange of the native oleate ligands for dipolar ligands with varying electronegativity.[25] In ITO NCs, varying the dipole of the ligands to an electron donating (withdrawing) group caused a concomitant rise (lowering) of the electron concentration while decreasing (increasing) the plasmonic volume fraction and consequently widening (narrowing) W_d. The inverse relationship between the electron concentration

and plasmonic volume fraction upon dipolar ligand exchange is counter to the positive correlation of these trends when tuning W_d synthetically by changing the doping concentration. In the case of an electron-donating ligand, a modest increase in the electron concentration is offset by a larger increase in the band bending, thus increasing E_{BI} and W_d. This anticorrelated tunability of the electron concentration and the plasmonic volume fraction has so far only been achieved by postsynthetic ligand exchange. Furthermore, depletion layer engineering can modulate inter-NC plasmonic coupling strength in assemblies. In ITO NC superlattices, we recently showed that the depletion layer weakens coupling, and this effect is tunable based on synthetic variation of W_d, providing an opportunity for modulating the optical properties of assemblies.[39]

The quantitative analysis of the depletion layer during postsynthetic electron transfer reactions and the following ligand exchange is made possible by fitting LSPR spectra with the Heterogeneous Ensemble Drude Approximation (HEDA) model.[28] The NCs are modeled with a plasmonic core having a free electron (Drude) dielectric function and a dielectric shell that represents the depletion layer. To find the W_d and electronic properties of the core (e.g., electron concentration, n_e), the fitting procedure intakes experimentally measured properties such as NC size, concentration, and size distribution, which introduces heterogeneous broadening of the spectrum. As a result, intrinsic electronic properties such as n_e, W_d, and optical mobility can be determined from simple benchtop ensemble spectra. Yet, the robust understanding of depletion layers in ITO NCs with regards to quantitative analysis, tuning strategies, and impacts on coupling has yet to be systematically extended to other metal oxide materials to discern the universality of depletion layer effects and identify opportunities for maximizing their impact and utility.

Among plasmonic metal oxides, doped CdO NCs are a compelling target for extending understanding since they are predicted by eq 1 to exhibit substantial depletion layers owing to a high ϵ_r[40] and E_{BI}.[16] The synthesis of doped CdO NCs with tunable size, doping concentration, and morphology, including spherical NCs that can most readily facilitate quantitative analysis of depletion effects, has been previously established.[33,40−43] In particular, In-doped CdO (ICO) NCs can possess high electron concentrations on the order of 10^{21} cm^{-3} and conductivities 2−5 times higher than ITO depending on the doping concentration because of their high optical mobility.[41] ICO NCs also have one of the highest quality (Q)-factors reported for metal oxide NCs, up to ~8,[41] in comparison with ~4 reported for doped In$_2$O$_3$ NCs.[22,44] Yet, the electronic structure of CdO presents challenges to quantitative analysis of depletion layers. In particular, the conduction band is nonparabolic, so the effective mass depends on E_F and therefore changes with doping concentration.[45,46] This feature convolutes the relationship between the electron concentration and LSPR peak position when applying existing analytical frameworks. Due to a nonparabolic conduction band, for example in InN NCs, the LSPR frequency was nearly invariant in response to oxidation decreasing the electron concentration, necessitating a revised, material-dependent model to describe the LSPR modulation.[47] In the case of ITO NCs, nonparabolicity effects have been considered, but the effect is minimal enough to be well approximated as a parabolic band structure.[26,48] In contrast, this approximation does not necessarily hold for the significant nonparabolicity of CdO-based NCs. Previous efforts to fit the
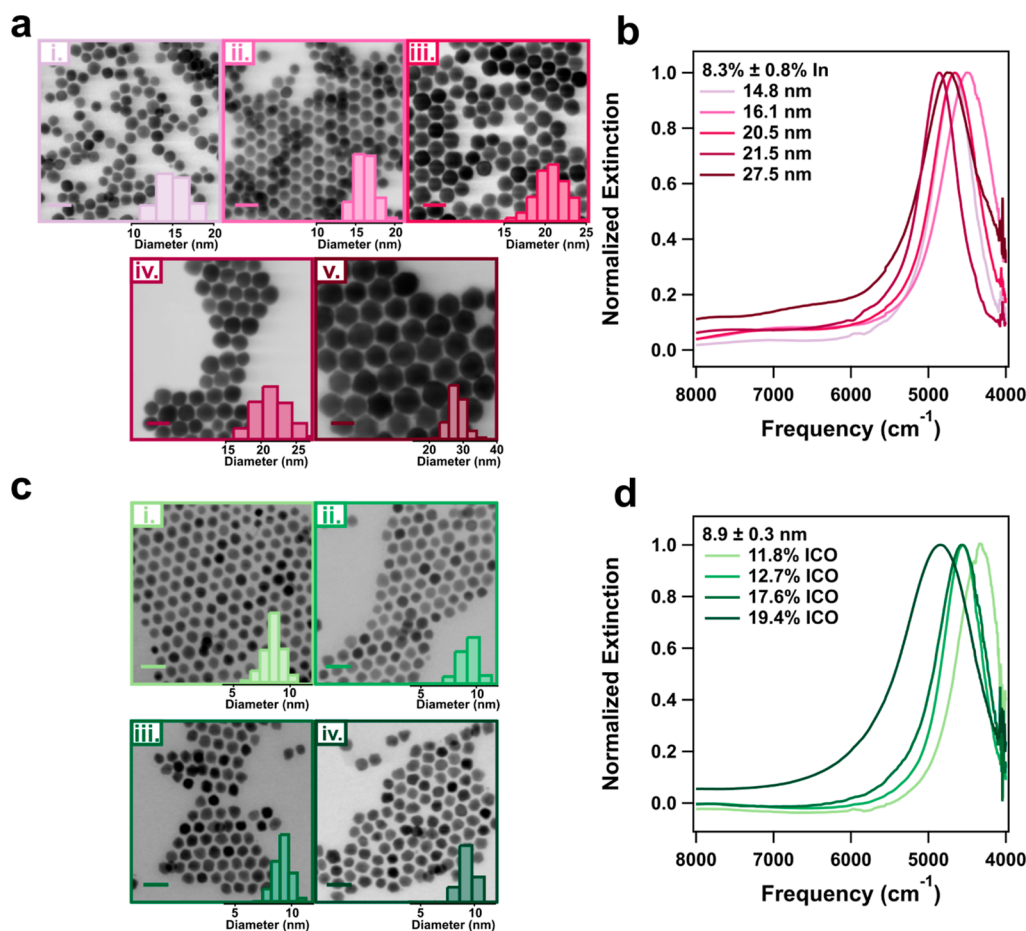
Figure 2. Materials characterization of ICO NC size and doping series. STEM images of ICO NCs: (a) size series at constant 8.3 ± 0.8% In and variable diameter as shown (insets show histograms of size distributions), (c) doping series at constant 8.9 ± 0.3 nm and variable % In as shown (insets show histograms of size distributions), and (b,d) associated extinction spectra of NC dispersions in a 1:1 mixture of tetrahydrofuran and toluene. Scale bars in (a) and (c) are 30 nm.

LSPR of doped CdO NCs have assumed a single, fixed effective mass despite changes in aliovalent doping concentration,[46,49] which can potentially introduce errors into the determination of n_e.

In this work, we advance the understanding of depletion layers in metal oxide NCs by systematically studying their effects on the optical properties of ICO NCs as a function of NC diameter, In doping concentration, and varying postsynthetic modifications. Using established techniques to synthetically tailor the diameter and doping concentration, we determine that increasing either parameter leads to decreases in the volume fraction occupied by the depletion layer, consistent with previous findings in ITO NCs. However, owing to the higher dielectric constant of CdO than In_2O_3 (5.5[40] and 4.0,[28] respectively), ICO NCs exhibit substantially wider depletion layers for the same diameter and doping concentration than do ITO NCs. Employing the aforementioned postsynthetic modifications, we determine that the wide depletion layer of ICO NCs and the nonparabolic conduction band profile causes a preferential change in the core electron concentration over the depletion layer, which consequently enables a wide dynamic range for LSPR modulation. Chemical reduction of ICO NCs produces large LSPR frequency shifts of up to 1700 cm^{-1}. Intrinsic NC properties are quantitatively tracked with a generalized HEDA model that is parametrized for use in materials with electronic band structures beyond the

prototypical case of ITO NCs. Spectral fitting results confirm the high degree of electron concentration tunability that contributes to wide optical modulation, while the change in the depletion layer as a function of reduction is modest. In contrast with the concomitant charging of the plasmonic core and depletion layer when reducing ITO NCs, the nonparabolic band structure of ICO NCs causes preferential charging of the plasmonic core over the depletion layer, demonstrating how band structure effects can be leveraged to radially control NC charging. Similar to chemical reduction, postsynthetic ligand exchange of the native oleate ligands results in larger spectral shifts in ICO than ITO NCs and reveals limited depletion layer modulation. By assembling the ICO NCs into superlattices and using the spectral shift as an indicator of LSPR coupling strength, we find that the wide intrinsic depletion layer in ICO NCs hinders coupling. However, we deliberately tune W_d via aliovalent doping to compress the wide depletion layer and, thus, strengthen inter-NC coupling. Overall, these results establish a more comprehensive understanding of ICO NCs' plasmonic properties and the influence of the depletion layer and suggest opportunities to leverage these phenomena for dynamic IR optical materials useful for applications such as sensing, photovoltaics, and electrochromics.

RESULTS AND DISCUSSION

The electronic structure and thus, depletion layer, can be synthetically controlled in doped metal oxide NCs using handles such as the diameter, doping concentration, morphology, and composition.[18] We used a previously reported method[41] to synthesize oleate-capped ICO NCs with varied sizes and doping to rationalize the impacts on the depletion layer. In brief, the synthesis involves thermal decomposition of a mixture of metal precursors in the presence of the surfactant oleic acid. The reaction mixture is quickly heated to reflux (315 °C) to produce small, spherical ICO NCs. The diameter can be tuned from 8 to 30 nm depending primarily on the molar ratio of oleic acid to total metal precursor, ranging from 2.5 to 4 to increase the NC diameter. The doping concentration was controlled by tailoring the stoichiometric ratio of Cd to In precursor; however the relative In concentration incorporated in the NCs was consistently greater than in the reaction mixture (Tables S1 and S2), which we ascribe to the loss of some Cd precursors to precipitation of Cd^0 during synthesis, similar to the formation of Cd^0 during CdTe NC synthesis.[50] We also observed a slight dependence of the NC diameter on the In doping concentration. Higher In doping resulted in slightly smaller NCs, which necessitated compensating with increased oleic acid for higher doped ICO to produce a consistent size while varying the doping concentration. Ultimately, we obtained a size series ranging from 14.8 to 27.5 nm at an average In doping of 8.3 ± 0.8% (Figure 2a,b) and a doping series with a near constant diameter of 8.9 ± 0.3 nm ranging from 11.8 to 19.4% In concentration (Figure 2c,d). Given that the diameters of all the samples used in this study ranged from 8.4 to 27.5 nm and the Bohr exciton radius of CdO-based materials has been estimated to be 2−4 nm,[51] we do not expect quantum confinement to play a role here.

To quantitatively understand the impact of In doping on the plasmonic response, the overall In doping concentrations and NC dispersion volume fractions were measured with inductively coupled plasma optical emission spectroscopy (ICP-OES), which established the near-constant In doping in the size series and the gradient in In found in the doping series. Furthermore, measuring the In doping concentration with X-ray photoelectron spectroscopy (XPS), a surface-sensitive technique, revealed a higher In concentration than ascertained by ICP-OES, indicating preferential surface segregation of the In dopants (Tables S1 and S2). The LSPR of each sample was measured with UV−vis−NIR spectroscopy and revealed very narrow spectral line widths, consistent with previous comparisons of doped CdO NCs to other conductive metal oxide NCs in the literature.[7] Increasing the ICO NC diameter led to a slightly increasing LSPR frequency, ω_{LSPR}, despite a gradual decrease in incorporated In concentration (Figure 2f). We attribute the increasing ω_{LSPR} to higher dopant activation in larger NCs (Table S1), similar to previous results in ITO NCs that have demonstrated how NC size, dopant distribution, and dopant activation can significantly influence the ω_{LSPR} and LSPR line shape.[19,52] Maintaining a constant NC diameter while increasing the In dopant concentration led to a higher ω_{LSPR}, consistent with increasing the electron concentration (Table S2). Note that although a broader range of In concentrations is synthetically accessible, it was necessary to use high In concentrations, particularly in this small doping series, to avoid significant

overlap between the ω_{LSPR} and solvent absorption bands that can frustrate accurate spectral analysis.

Reducing Titrations. To evaluate the effects of NC charging on the depletion layer and plasmonic response, each ICO NC dispersion was postsynthetically reduced with decamethylcobaltocene ($CoCp_2^*$). To briefly summarize the reduction process, $[H(OEt_2)_2]^+[BAr_4^F]^-$, a proton source known as Brookhart's acid,[53] was first added to the NC dispersion in a 1:1 mixture of tetrahydrafuran (THF)/toluene to provide charge compensation to the electrons added upon reduction. Despite the acid sensitivity of CdO, the NCs remained colloidally dispersed with little change in the LSPR observed. Then, 10, 5 μL additions of 6.7 mM $CoCp_2^*$ solution in the same THF/toluene mixture were added to the NCs, measuring the extinction spectrum after each addition. Reducing titrations were repeated in triplicate for each ICO NC sample and found to be highly reproducible (Figure S1). $CoCp_2^*$ induced a gradual blue-shift of the LSPR until the shift eventually saturated (Figure 3a). Particularly in smaller NCs, we observed slight destabilization of the NC dispersion upon the first addition of $CoCp_2^*$, which caused LSPR broadening; however, the narrow line width was quickly recovered with the second $CoCp_2^*$ addition and persisted through the maximally reduced state, indicating that the NCs maintained colloidal stability at high reduction levels (Figure S2). As a check on reversibility of the reduction process, ICO NCs were first partially reduced with $CoCp_2^*$ to prevent excess $CoCp_2^*$ in solution and then oxidatively titrated with $[FeCp_2]^+$ (Figure S3), as previously done on reduced ITO NCs.[17,29] However, unlike ITO NCs, not all of the $CoCp_2^*$-added electrons were able to be oxidatively extracted by $[FeCp_2]^+$, as evidenced by the LSPR not returning back to the as-synthesized frequency, even after excess $[FeCp_2]^+$ was added. This result could be indicative of two scenarios; first, some irreversible reduction of Cd^{2+} to Cd^0 could be occurring that prevents some degree of subsequent oxidation. Second, the $[FeCp_2]^+$ redox potential may be above the as-synthesized NC E_F, such that $[FeCp_2]^+$ is thermodynamically unable to oxidize all of the $CoCp_2^*$-added electrons, and hence, suggesting that the as-synthesized ICO NC E_F is at a lower absolute potential than the as-synthesized ITO NC E_F. Indeed, we observed no apparent transfer of electrons from as-synthesized ICO NCs to $[FeCp_2]^+$ (Figure S4). Regardless of the reversibility of the reduction process, the optical and electronic impacts of NC reduction can still be analyzed both qualitatively and quantitatively.

The dynamic range of the LSPR under reducing titrations is quantified by the frequency difference between the LSPR in the as-synthesized and maximally reduced states ($\Delta\omega_{Titr}$). Examining $\Delta\omega_{Titr}$ in relation to the NC diameter and In doping concentration revealed an inverse correlation, qualitatively consistent with previous observations in ITO NCs[13,14] (Figure 3b,c). Here, the $\Delta\omega_{Titr}$ is independent of the amount of $CoCp_2^*$ added to the NCs because $CoCp_2^*$ is in sufficient excess by the end of each titration that no further peak shift is apparent with the addition of further $CoCp_2^*$ (Figure S5). Notably, ICO NCs have a significantly greater dynamic range for LSPR tuning as compared to ITO NCs. For example, 9.0 nm, 12.4% In ICO NCs experienced a 1700 cm^{-1} blue-shift, whereas comparable 8 nm, 13% Sn ITO NCs were previously reported to have a maximum LSPR shift of only 750 cm^{-1}.[14] Had it been feasible to use lower In doping concentrations here, we expect the dynamic range of LSPR modulation exceeding 2000 cm^{-1} to be attainable for ICO NCs. We
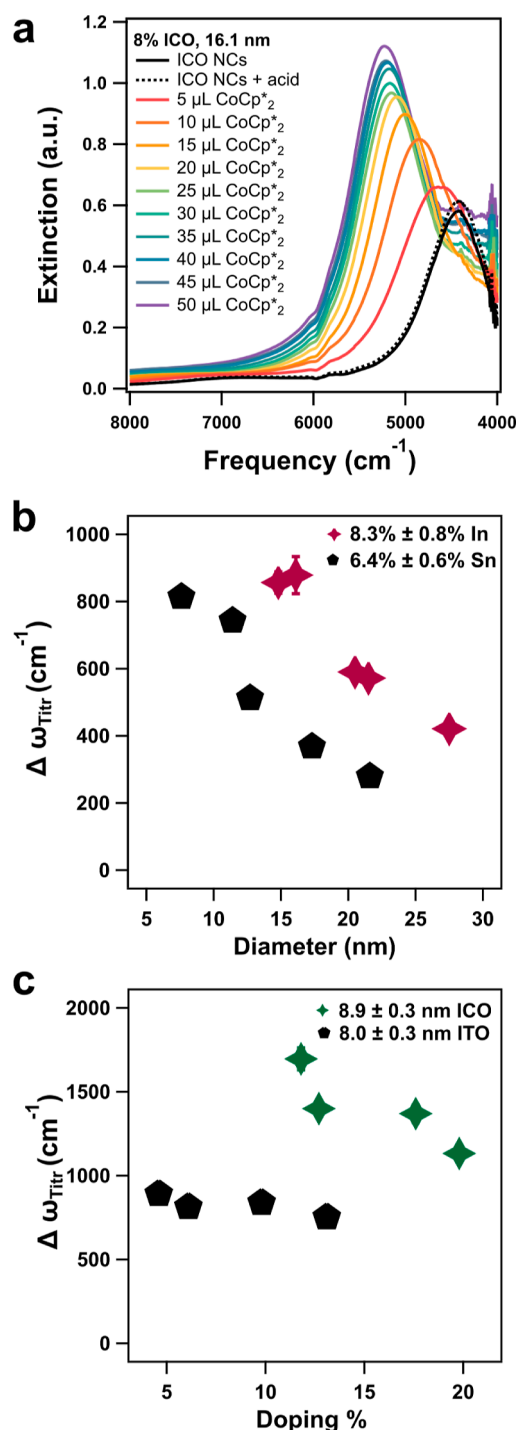
Figure 3. Reducing titration results of size and doping series, using ITO NCs as a comparison. (a) Example of reducing titration of 16.1 nm, 8.1% ICO NCs with 10 additions of $CoCp_2^*$, spectra have been adjusted to account for dilution. Frequency difference between the as-synthesized (black line) and maximally reduced (purple) NCs corresponds to $\Delta\omega_{Titr}$ and is compared for ICO and ITO NCs at similar (b) NC diameter and (c) In and Sn doping concentration. ITO data are from ref 14 ITO NCs are black hexagons, and ICO NCs are pink and green stars.

quantitative analysis of the changes occurring during titration to test this hypothesis.

The electronic properties of the as-synthesized and chemically reduced NCs were deduced by fitting the dispersion LSPR spectra with the HEDA model. Fitting parameters include the mean and standard deviation of the electron concentration (μ_{n_e} and σ_{n_e}, respectively), volume fraction of the plasmonic core (f_e), and the bulk mean free path (l_{bulk}) of an electron in the NC. Previous analyses of changes in the depletion layer as a function of NC diameter, doping concentration, reduction, or ligand exchange have been restricted to In_2O_3-based NCs.[14,17,25,28,54] Adapting the HEDA model to enable the spectral analysis of ICO NCs requires a revision of the underlying model to account for the nonparabolicity of the CdO conduction band. Usefully, enabling user-defined variables to accommodate different electronic band structures broadens the applicability of the HEDA model to more plasmonic semiconductor materials. The nonparabolic conduction band in ICO renders the electron effective mass, m_e^*, dependent on the Fermi level and therefore on n_e, which makes it difficult to deconvolute the impacts of each electronic parameter on the LSPR frequency. To account for this complication in as-synthesized NCs with varying doping concentrations, we first determined the optical bandgap, E_g, from Tauc analysis (Figure S6) and employed previously reported empirical models for CdO-based NCs that relate m_e^* to E_g.[55,56] It was also necessary to account for changes occurring in m_e^* throughout the reduction process since the conduction band bending changes as E_F ascends further into the conduction band. To account for the changing m_e^* as a function of successive $CoCp_2^*$ reduction, the potential n_e values were tabulated in a look-up table together with their associated m_e^* values calculated based on experimentally established relationships between n_e and m_e^*.[56] As the fitting process proceeds, the value of m_e^* is iteratively updated and remains tied to the trial value of n_e. Once the mean n_e is determined from the fitting process, the associated m_e^* is extracted as the final m_e^*. Fixing the relationship between m_e^* and n_e rather than floating m_e^* independently avoids adding another fit parameter and instead explicitly accounts for the nonparabolic electronic structure of doped CdO without overparameterizing the model. Additionally, the high electronic mobility and thus low damping constant that distinguish ICO necessitated alteration of the treatment of surface damping in the HEDA model. Briefly, a theory-dependent proportionality constant, A, included in the surface damping term, was decreased from $\frac{3}{4}$ classically used in ITO to $\frac{1}{4}$ in ICO to account for the lower damping rate (Figure S7). A detailed explanation of the updates made to the HEDA model and fittings of all reducing titration spectra (Figure S8) is included in the Supporting Information, and the updated code is publicly available.

HEDA fitting of the LSPR of the as-synthesized particles (0 μL $CoCp_2^*$) quantitatively revealed the intrinsically wide depletion layers present in ICO NCs despite the high doping concentrations measured with ICP-OES. Furthermore, the slight In surface segregation revealed by XPS (Tables S1 and S2) means that the substantial depletion layer widths we observed here might be even larger were the dopants uniformly distributed since surface segregation of dopants has been shown to diminish depletion layer widths.[16,20,21,57,58] Consistent with eq 1 and with previous results for ITO NCs,[28] we

hypothesized that the extreme optical modulation in ICO NCs results from the intrinsically wide depletion layer providing the capacity for a greater extent of reduction, motivating a more
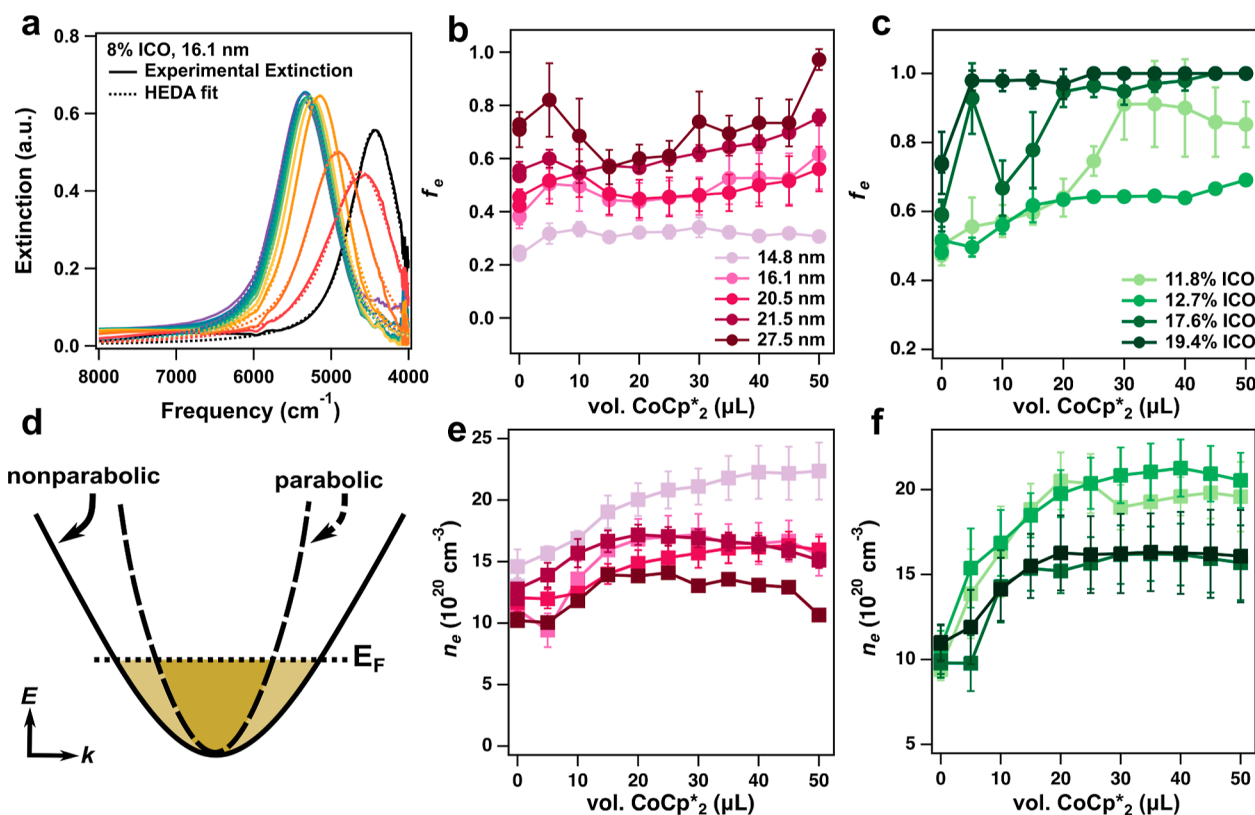
Figure 4. In situ HEDA fitting results of reducing titrations in ICO NC size and doping series. (a) Example of experimental spectra (solid lines) and respective HEDA fits (dotted lines) for 16.1 nm, 8% ICO NCs. Plasmonic core volume fraction (f_e) throughout reducing titrations in (b) size and (c) doping series. (d) Schematic of nonparabolic (solid line) and parabolic (dotted line) conduction band profiles. Electron concentration (n_e) throughout reducing titrations in (e) size and (f) doping series.

observe that f_e (inversely correlated to W_d) increases as a function of diameter, which we rationalize as an approximately constant W_d but higher core volume fraction. Deviations from a constant W_d in the size series can be attributed to modest variations in the In doping level. For increasing In doping concentration in the doping series, the growing f_e corresponds to a narrowing W_d (Figure S9). Despite the relatively high In doping concentration and large size of our NCs, we calculate a maximum plasmonic core volume fraction of only 0.75 in the most extreme cases (19.4% In sample and 27.5 nm sample). This is in stark contrast to ITO NCs, wherein the depletion layer is nearly eliminated in samples larger than 12 nm and NCs doped above 6% Sn.[14,28] The wide depletion layer in ICO NCs can be primarily attributed to the higher ϵ_R in the material; however, a lower flat band E_F and thus higher built-in potential, E_{BI}, may also be significantly contributing, as has previously been hypothesized for CdO-based NCs.[16]

Fitting the successive spectra collected throughout the titration (Figure 4a) of the ICO size and doping series revealed how the nonparabolic band structure of ICO plays a critical role in depletion layer tuning and LSPR modulation. In nearly all ICO NC samples, f_e modestly increases throughout the titration but does not reach the point at which the depletion layer is eliminated ($f_e = 1.0$) before reduction saturation is reached (Figure 4b,c). Again, this is in contrast with the depletion layer charging dynamics of ITO NCs, where the depletion layer was rapidly filled with electrons early in the reduction process, effectively filling the whole NC volume with plasmonically active free electrons.[14] The gradual depletion layer filling in ICO is particularly notable in conjunction with

the drastic increase in n_e throughout the reduction process (Figure 4e,f), adding up to 10^{21} electrons per cm^3, which can be converted to an absolute number of electrons by scaling the NC diameter by f_e (Figure S10). In short, the chemically titrated additional electrons primarily first fill the depletion layer in ITO NCs, while they instead substantially populate the plasmonic core in ICO NCs.

The limited depletion layer tunability yet wider optical modulation range, $\Delta\omega_{Titr}$, suggests a broadened conduction band profile at higher energies, consistent with the non-parabolic conduction band in ICO.[45] In comparison to a parabolic conduction band (such as the case for ITO NCs), the density of states increases more rapidly above the conduction band edge for a nonparabolic conduction band, so a higher electron concentration is necessary to fill the band and increase E_F (Figure 4d). The depletion layer width is tied to the NC E_F through E_{BI}, hence the more limited tunability of the depletion layer despite significant levels of reduction. A thorough analysis of the limitations on the maximum n_e reached and the subsequent implications for ICO NC charging dynamics and band structure is included in the Supporting Information (Figures S11 and S12) but is not the focus of the present discussion.

Dipolar Ligand Exchange. Postsynthetic ligand exchange of native oleates with dipolar ligands is another strategy to manipulate plasmonic response and spatial distribution of electrons in semiconductor NCs by tuning the ligand's dipole moment.[25,59,60] Cinnamic acid ligands are well suited for studying the impacts of molecular dipoles on NC properties because they can partially exchange with native oleate ligands

while retaining colloidal NC stability, and the dipole moment can be readily tuned by varying the end group in the aromatic ring. A recent study on ITO NCs considered the electrostatic impacts of cinnamic acid ligands with various dipole moments on the NC plasmonic properties, using the HEDA model to deconvolute the relationship between dipole moment and depletion layer changes.[25] Electron withdrawing (donating) ligands induced an upward (downward) potential step at the NC surface, which decreases (increases) the band bending. The lower (higher) degree of band bending decreases (increases) E_{BI} and thus decreases (increases) W_d, consistent with eq 1.

To understand how the effect of molecular surface dipoles depends on NC composition and the electronic band structure, the native oleate ligands on 9.0 ± 1.1 nm, 17% ICO NCs (Figure S13) were postsynthetically partially exchanged with an electron-donating ligand, cinnamic acid (4H), and an electron-withdrawing ligand, 3,5-difluorocinnamic acid (3,5F).[25] The ligand exchange procedure was modified from that used for ITO NCs by the addition of a N,N-diisopropylethylamine (DIPEA) base, which does not interact with the surface but is used to prevent ICO NC dissolution by maintaining a neutral pH during the ligand exchange. Briefly, as-synthesized ICO NCs were precipitated and redispersed in a 0.05 M cinnamic acid ligand solution using chloroform (4H case) or ethyl acetate (3,5F case). After NC redispersion, the DIPEA base was added, in a 1:1 ratio to the ligand solution, and the solution was left stirring for 48 h. Ligand exchange induced a change in surface polarity, evidenced by NC precipitation with nonpolar solvents, and the resulting NC pellet was redispersed in chloroform for the 4H ligand and ethyl acetate for the 3,5F ligand. While we do not expect complete ligand exchange, successful cinnamic acid functionalization was confirmed by nuclear magnetic resonance (NMR) spectroscopy (Figure S14). Furthermore, the shifts in NC work function (Figure 5 and Table S3) observed by the secondary electron cutoff in ultraviolet photoelectron spectroscopy (UPS) also confirm ligand exchange.

The extinction spectra of the as-synthesized and ligand-exchanged ICO NCs revealed a red-shift in the LSPR for both the electron-withdrawing and electron-donating cases (Figure 5b). However, directly interpreting the LSPR peak frequency correlation with the ligand dipole moment would be misleading since the dispersing solvents are necessarily different and the dielectric constant of the medium (ϵ_M) influences the peak frequency. To resolve these convoluted factors, the extinction spectra were fit with the HEDA model to isolate and quantify the impacts of the ligand dipole moment on the optical and electronic properties, again accounting for the nonparabolic conduction band as described above. Consistent with previous results for ITO NCs, the electron-withdrawing character of the 3,5F ligand decreases W_d and increases f_e, while the reverse is true for the electron-donating 4H ligand (Figures 5c and S16). Increased f_e upon 3,5F ligand exchange suggests that electron-withdrawing ligands lower E_F, thereby decreasing the band bending potential (E_{BI}), which is consistent with the upward potential energy step at the surface indicated by the increased work function observed in UPS. Referring back to the Poisson's W_d equation (eq 1), lowering E_{BI} will decrease the W_d, and thus increase the electron accessible volume fraction, f_e. Moreover, 3,5F ligand exchange decreases n_e, further supporting the lowered E_F as a consequence of the upward potential step from
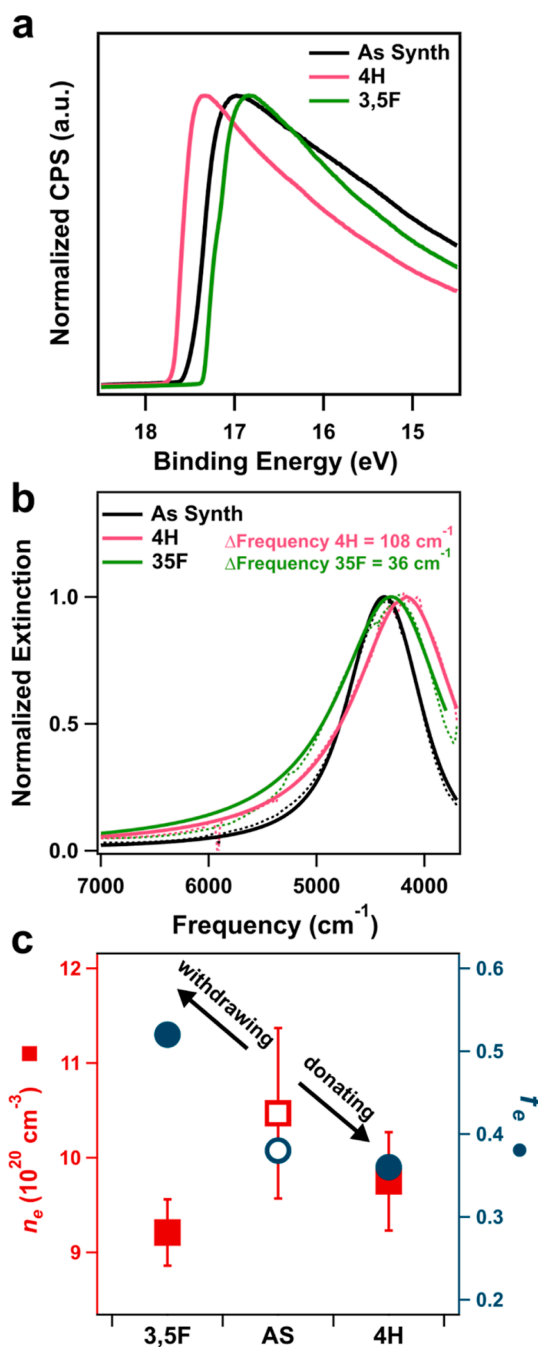

Figure 5. Characterization of as-synthesized and ligand-exchanged ICO NCs. (a) Secondary electron cutoff region of UPS spectra. (b) Normalized extinction spectra. Experimental spectra are shown in dotted lines, HEDA fits are overlaid in solid lines. (c) Change in f_e (circles) and n_e (squares) for as-synthesized (open symbols) and cinnamic acid ligand-exchanged (filled) NCs.

the electron-withdrawing ligand (Figure 5c). Recalling that the change in N_e reflects both changes in f_e and n_e, N_e increases upon 3,5F ligand exchange (Figure S17). All of these consequences for the electronic structure were found to be reverse in the electron-donating 4H case. Specifically, f_e was reduced, n_e grew, and N_e decreased following ligand exchange. These trends all qualitatively follow the behavior observed when dipolar cinnamate ligands were bound to ITO NCs, and their impacts were analyzed by UPS and HEDA spectral analysis.

The 4H and 3,5F ligands used here were chosen to demonstrate the effects of dipoles on the depletion layer and LSPR in ICO NCs and to evaluate the realization of previously observed phenomena in another metal oxide material. Comparing the results presented here for ICO NCs to previous ligand exchange of ITO NCs with the same ligands, the same qualitative trends in f_e, n_e, and N_e persist for ICO NCs.[25] In particular, the anticorrelated trend of f_e and n_e, distinct from their positive correlation based on variations in doping concentration, is observed in ICO NCs. Comparing the magnitude of the changes in the LSPR frequency and the electronic structure parameters obtained through HEDA analysis, we find that the LSPR shifts more substantially for ICO NCs, up to 108 cm^{-1} for the 4H case compared to 50 cm^{-1} in ITO NCs (Figure S18). Considering that the extinction measurements for the 4H-exchanged ITO and ICO NCs are in the same solvent (chloroform), the greater LSPR modulation observed in ICO NCs can be directly attributed to the more sensitive response of n_e to the dipolar ligands. Based on HEDA spectral analysis, ICO NCs experienced greater change in n_e, increasing by 1.26×10^{20} cm^{-3}, compared to 0.96×10^{20} cm^{-3} in ITO NCs, following exchange with the 3,5F ligand. In contrast, f_e changed more modestly in ICO NCs, decreasing by only 0.14, compared to 0.37 in ITO NC functionalization with 3,5F ligands.

These trends in the dynamic range of f_e and n_e going from as-synthesized NCs to exchange with the 3,5F ligand in the most extreme case can be related to the differences in how ITO and ICO NCs respond to chemical reduction. The wide, nonparabolic conduction band of ICO means that despite significant changes to the n_e induced by either ligand exchange or chemical reduction, W_d and, thus, f_e are less significantly perturbed than in parabolic conduction band materials such as ITO NCs. The larger E_{BI} of ICO NCs supplies a thermodynamic driving force for electrons to be preferentially shuttled to the plasmonic core, where they contribute to increasing n_e, rather than progressively filling the depletion layer.

Coupling in Nanocrystal Superlattices. Like other plasmonic nanoparticles, when doped CdO NCs are assembled into superlattices with long-range order, their LSPR modes couple, giving rise to a collective plasmon resonance (CPR) at a lower frequency. Where strong enough coupling occurs, these assemblies can exhibit a negative real part of the effective dielectric response, which produces a metal-like optical response.[41,61] However, the effects of the depletion layer on the strength of the coupling have yet to be examined in doped CdO NCs. Plasmonic coupling between NCs depends on the NC size and spacing between neighboring NCs, which govern the extent to which the induced dipole of each NC will polarize the surrounding NCs leading to a collective, hybridized resonance mode for the superstructure. It has been established that larger NCs or smaller gap distances between NCs will lead to stronger coupling effects due to stronger induced electric field interactions.[62−65] We have recently analyzed how depletion layers moderate the plasmon coupling strength in ITO NC superlattices,[39] finding that these insulating layers cause weaker induced electric field interactions leading to lower plasmonic coupling strength. Considering that the electron concentration and radial distribution within each NC play a strong role in plasmon coupling, we reasoned that the intrinsically wide depletion layer in ICO NCs could hinder NC coupling beyond what we observed for ITO NCs.

To assess the impacts of the depletion layer on ICO NC coupling, 16.9 ± 1.5 nm ICO NCs were assembled into superlattices with previously reported techniques,[66,67] where a NC dispersion in toluene was slowly evaporated to deposit NCs onto a silicon substrate, resulting in ordered superlattice films after 10 days. Long-range order and hexagonal packing were apparent from top-down imaging of the superlattices with scanning electron microscopy (SEM, Figure 6a). NC packing density, interparticle spacing, and order were assessed with grazing incidence small-angle X-ray scattering (GISAXS)
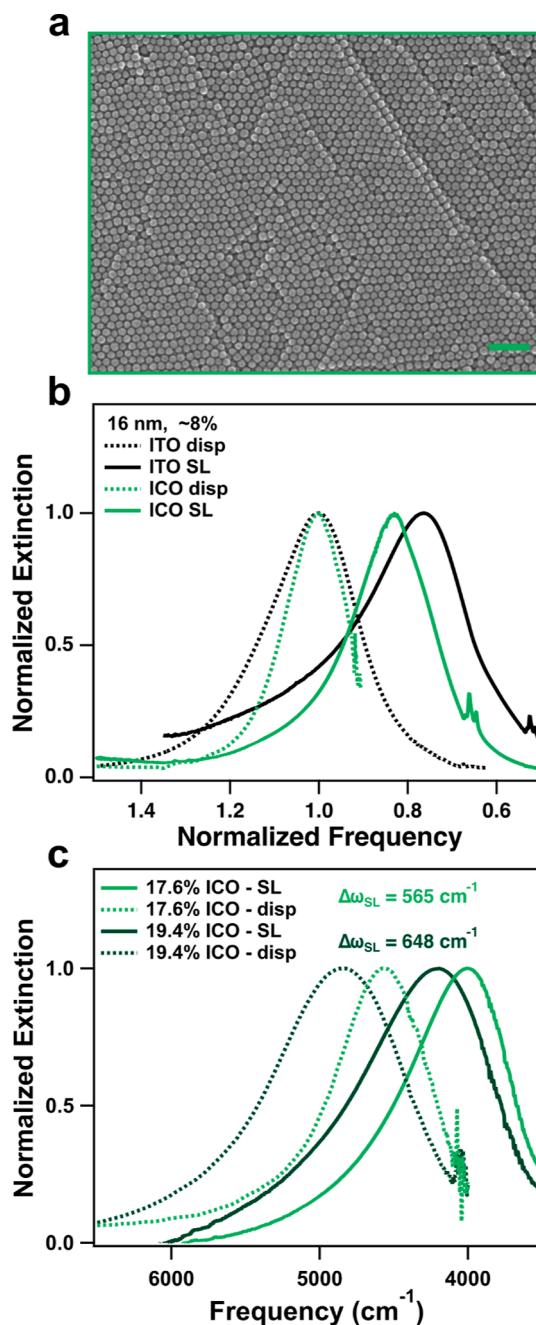

Figure 6. (a) SEM image of the assembled superlattice of 16.9 nm ICO NCs. Scale bar is 100 nm. (b) Extinction spectra normalized by corresponding dispersion frequency (dotted line) of 15.7 nm, 8% ITO and 16.9 nm, 8% ICO NC superlattice samples (solid line). (c) Extinction spectra of dispersions and superlattices of ICO NCs at 9.0 nm, 17.6% In and 9.2 nm, 19.4% In.

analysis of the superlattices, which revealed face-centered cubic (FCC) ordering (Figure S19), typical of oleate-capped NC assemblies. The spacing between indexed peaks and the average NC size determined by small-angle X-ray scattering of a dilute dispersion (Figure S20) was used to calculate a gap distance of 4.4 nm between neighboring NCs for the ICO superlattices. The gap distance between NCs is primarily dictated by surface chemistry, such as the density or interdigitation of the surface ligands. Given the consistent oleate capping expected for the ICO NCs used in the superlattice assembly, the NC spacing is assumed to be constant as the NC size and doping concentration are varied.

Spectral shift from the LSPR of isolated NCs to the hybridized CPR mode of a superlattice upon assembly ($\Delta\omega_{SL}$) can be used to assess the coupling strength.[62,64,68,69] Hence, a larger $\Delta\omega_{SL}$ between the dispersion and superlattice spectra corresponds to greater coupling in the superlattice. Using ITO NCs as a benchmark to evaluate the impact of the depletion layer in ICO NCs of comparable size (15.7 ± 1.3 nm), doping concentration (8%), and gap spacing (4.7 nm), we observed a $\Delta\omega_{SL}$ of 1323 cm^{-1} for ITO versus 768 cm^{-1} for ICO (16.9 ± 1.5 nm diameter, 8% doped, 4.4 nm gap spacing), indicating weaker coupling in the ICO NCs (Figure S21). Since these NCs are all similarly oleate-capped, the separation or gap distance between neighboring NCs is approximately constant; therefore, we posit that the wider depletion layer in the ICO NCs than ITO NCs (2.2 nm vs near zero) weakens the electric field interactions between the plasmonic cores and decreases inter-NC LSPR coupling. Although the ITO and ICO NCs were of similar size and doping concentration, the LSPR frequencies of the dispersed NCs differed, which can also contribute to a difference in $\Delta\omega_{SL}$. To account for this difference, we normalized the spectra by the peak LSPR frequency of the corresponding dispersions, which reveals an even larger difference between the coupling-induced shift in ITO and ICO NC superlattices (Figure 6b). This comparison suggests that coupling in ICO NC superlattices should be tunable based on synthetically controlled variations in the depletion layer. So, we varied aliovalent doping in 9 nm ICO NCs, increasing the In dopant concentration from 17.6 to 19.4%, which narrowed W_d from 0.73 to 0.43 nm based on HEDA fitting of the NC LSPR spectra. The $\Delta\omega_{SL}$ increased from 565 to 648 cm^{-1} (Figure 6c), and the trend persisted even when normalized to the dispersion frequency (Figure S22), demonstrating stronger coupling with a thinner depletion layer. Importantly, the results presented here suggest that the electron distribution plays an even stronger role in determining the coupling strength than does the electron concentration in the plasmonic core. This is evidenced by weaker coupling in ICO than in ITO NC superlattices; despite the intrinsically higher electron concentration, the separation between plasmonic cores imposed by the depletion layer hinders the coupling overall.

The inverse correlation between depletion layer width and spectral shift upon assembly demonstrates that depletion layer engineering is a viable strategy to tune the plasmonic response not only for dispersed NCs but also in assemblies and to enhance the intrinsically weak coupling exhibited by ICO NCs. We expect that other postsynthetic depletion layer tuning techniques, including those described here, would have a similar effect on coupling, although experimental factors such as excess redox reagents in postsynthetically doped NCs or altered surface chemistry in ligand-exchanged NCs could

potentially convolute the impacts of the depletion layer on coupling and make quantitative interpretation challenging. Despite the myriad of beneficial properties noted in ICO as a low loss plasmonic material, the intrinsically wide depletion layers may pose a challenge for applications that require strong coupling; this limitation could be rectified with the depletion layer engineering strategies from molecular dipoles to redox doping, or, in the future, controlling the radial distribution of dopants.[21,58]

CONCLUSIONS AND OUTLOOK

In summary, we have demonstrated how various plasmon modulation strategies can be applied to ICO NCs to elucidate the effects of the depletion layer on optical and electronic properties and to generalize concepts developed to rationalize the behavior of ITO NCs. We show that ICO NCs have an intrinsically wide depletion layer, owing to the high ϵ_R and E_{BI}, and that the relative impact of the depletion layer can be synthetically controlled by altering the NC diameter and In doping concentration. Quantitative analysis of the depletion layer was enabled by a generalized spectral fitting model that was updated to incorporate distinctive band structures and postsynthetic modifications. Leveraging this fitting model in postsynthetic depletion layer tuning strategies, chemical reduction across sizes, and In doping levels in ICO NCs revealed that while n_e, and thus, the LSPR peak, can be broadly varied, there is relatively little change in the width of the depletion layer. These results are a consequence of the nonparabolic band structure previously reported for ICO.[45,46] Furthermore, exchanging oleate ligands with dipolar ligands, which alters the extent of radial band bending, provides another way to tune the LSPR and depletion layer. Comparing these depletion layer tuning techniques in ICO NCs to the canonical plasmonic metal oxide, ITO, revealed that although the depletion layer tuning range is more limited in ICO NCs, the breadth of plasmon modulation is significantly enhanced. To study the impacts of the depletion layer on LSPR coupling, ICO NCs were assembled into superlattices, where they displayed weaker coupling than ITO NCs due to the spatial confinement of free electrons to a smaller plasmonic core. However, depletion layer tuning by doping was used to compress the depletion layer and enhance the inter-NC coupling. Overall, this study revealed that the nonparabolic conduction band in ICO plays a significant role in the radial distribution of electrons upon postsynthetic modification and enables broad plasmonic tunability. Despite the intrinsically wide depletion layer in ICO, various strategies are effective in tuning the depletion effects and mitigating this potential pitfall for its application in photonic materials and devices requiring strong coupling. Considering that ICO thin films are already of significant interest as transparent conductive films,[42,70,71] future work might explore how depletion layer engineering can be used to enhance electronic coupling and prevent electron transport bottlenecks due to contact resistance in ICO NC films.[58,72,73] Furthermore, studying depletion layer tuning in anisotropic semiconductor materials, where the Fermi level pinning can be facet dependent,[12,74] would contribute to the understanding of the role that the depletion layer plays in optical and electronic performance metrics such as conductivity, plasmonic "hot spot" generation, and optical modulation.

EXPERIMENTAL METHODS

Chemicals. The following chemicals used to synthesize ICO NCs were purchased commercially and were not further purified upon use: Cadmium acetylacetonate (Sigma-Aldrich, ≥99.99%), indium(III) acetate (STREM, ≥99.99%), oleic acid (Sigma-Aldrich, ≥90%), and 1-octadecene (1-ODE, Sigma-Aldrich, 90%) as synthesis reactants. Ethanol (Fischer Chemical, ≥90%), tetrahydrofuran (Sigma-Aldrich, ≥99.9%), and toluene (Sigma-Aldrich, ≥99.9%) were used to precipitate and disperse the NCs. For chemical reduction, sodium tetrakis[3,5-bis(trifluoromethyl)phenyl]borate and bis-(pentamethylcyclopentadienyl)cobalt(II) were purchased from Sigma-Aldrich and dried under vacuum at 100 °C for 16 h prior to use. *Trans*-cinnamic acid (4H, Sigma-Aldrich, ≥99%) and *trans*-4-(trifluoromethyl)cinnamic acid (CF3, Sigma-Aldrich, 99%). For ICP-OES, the standards used were cadmium and indium ICP standards (Sigma-Aldrich, 1000 mg/L ± 2 mg/L).

Nanocrystal Synthesis and Purification. In a 100 mL round-bottom flask attached to a Schlenk line, 2.5 mmol of total metal precursor were loaded into the flask with the molar ratio of Cd to In precursor reflecting the targeted In doping concentration. Oleic acid (6.25−10 mmol) and 30 mL of 1-ODE were added to the flask as a capping agent and solvent, respectively. The reaction was heated to 120 °C under N_2, at which 3−30 min degas cycles were performed with 2 min N_2 cycles between cycles. The reaction flask was then turned to N_2, wrapped with glass wool, and quickly heated to 320 °C. Within 30 min of the reaction reaching at least 312 °C, it changed its color from pale yellow to a dark green/brown, indicative of NC nucleation. Cd metal was formed during each synthesis, although the ratio of the Cd precursor that formed Cd^0 rather than NCs varied with each synthesis. After 30 min of stirring the reaction at 315−320 °C, it was quickly cooled with an air gun to room temperature. During the cooling period, 4 mL of room-temperature toluene was injected into the flask. Once the reaction had cooled to room temperature, it was transferred to a centrifuge tube, 20 mL of ethanol was added, and the solution was centrifuged at 9000 rpm for 10 min. The pellet of NCs was redispersed in 10 mL of toluene, appearing cloudy and dark gray/brown due to Cd^0 in solution. The solution was centrifuged at 2000 rpm for 2 min to separate the Cd^0 from the colloidally dispersed NCs, which were in the clear supernatant layer. The supernatant was decanted into another centrifuge tube and washed three times where each wash constituted precipitation of the NCs with ethanol, centrifuging at 9000 rpm for 8 min, and redispersing the NC pellet in 5 mL toluene. Following these 3 washes, aggregates were separated a final time by centrifuging the dispersion at 2000 rpm for 2 min and filtering the supernatant with 0.45 μm PVDF filter.

Characterization. *Scanning Transmission Electron Microscopy.* Colloidal ICO NCs were imaged on a Hitachi S5500, accelerating voltage of 30 kV, and 10 mA beam current operating in bright field STEM mode. Samples were prepared by dropcasting 8 μL of dilute ICO NCs in toluene solution on a Cu 400 mesh TEM grid. The grid was dried at least overnight in a vacuum desiccator. ImageJ was used to determine the NC diameter from the STEM images, analyzing at least 400 NCs per sample. Nanocrystal superlattices were imaged on the Si wafer they were assembled on at an accelerating voltage of 30 kV and 15 mA beam current operating under scanning electron secondary electron (SE) mode to assess top down/surface ordering.

Inductively Coupled Plasma-Optical Emission Spectroscopy. ICO NC dispersion volume fractions and In doping concentrations were determined by measuring In and Cd concentrations of the digested solutions on an Agilent 5800 ICP-OES. Diluted solutions were prepared by drying a known amount of ICO NC stock solution and digesting the NC pellet in aqua regia for at least 48 h. Digested NCs were diluted with Milli-Q water to a final acid concentration of 2%. Standard solutions containing known amounts of In and Cd standards were prepared with 2% (v/v) nitric acid and Milli-Q water. The In doping concentration was calculated by dividing the measured In concentration by the total metal concentration (Cd + In). The ICO volume fraction in the stock dispersion was determined by calculating the NC concentration from the ICP-OES measured metal content and converting this to a volume fraction using the density of CdO, 8.15 g/mL.

Photoelectron Spectroscopy Techniques. XPS and UPS measurements were performed on a VersaProbe 4 X-ray Photoelectron Spectrometer instrument. For as-synthesized and ligand exchanged samples, ICO NC dispersions were dropcast onto a p-doped silicon substrate, and the solvent was allowed to evaporate overnight. Once transferred to the instrument, samples were measured using Al Kα radiation ($\lambda = 1486.6$ eV) for XPS and a He (I) source (21.22 eV) for UPS. In the XPS experiment, near-surface doping percentages were calculated by taking the ratio of integrated area under the In 3d peak to the sum of the Cd 3d and In 3d peaks while taking into consideration their respective relative sensitivity factors. For the UPS experiment, the work function and ionization energy of the ligand exchanged ICO NCs were obtained as previously described.[25]

Small Angle X-ray Scattering and Grazing Incidence Small Angle X-ray Scattering. The SAXSLAB Ganesha instrument in the Texas Materials Institute at the University of Texas at Austin was used to collect the SAXS and GISAXS scattering patterns for the ICO NC dispersions and superlattices. The sample−detector distance was approximately 1 m, and a silver benzoate standard was used for both measurements. SAXS samples were measured in epoxy-sealed capillary tubes (Charles Supper Company, Inc.) in transmission mode. The SAXS data were processed using Igor Pro-based Irena and Nika software; the scattering pattern of the dispersion was fitted with a spheroid form factor to determine the ITO NC size. GISAXS scattering patterns were collected in grazing incidence mode at an incidence angle of 0.200° and used to obtain packing order and interparticle spacing.[75]

Reducing Titration. All reagents and NCs used in chemical titrations were prepared under air-free conditions in an Ar-filled glovebox. CoCp$_2^*$ solution was prepared by dissolving the previously dried CoCp$_2^*$ in 1:1 THF/toluene to a 6.7 mM concentration, stirring at 800 rpm overnight, and filtering the solution with a 0.45 μm PVDF filter. Despite filtering, some CoCp$_2^*$ powder settled out of solution over time meaning that the final concentration was likely less than 6.7 mM. $[H(OEt_2)_2]^+[BAr_4^F]^-$, Brookhart's acid, was prepared according to previous literature reports[53] and diluted to a 0.02 M concentration in THF with 30% of the solution by volume consisting of an equal mixture of oleic acid and oleylamine to stabilize the NCs during reduction. In solution, a portion of the oleylamine is most likely converted to oleylammonium by Brookhart's acid; however, this does not impact the overall analysis of the $\Delta\omega_{LSPR}$ in titrations because the Brookhart's acid is added in such excess of the NCs (Figure S5).

Each ICO NC dispersion was prepared in a glovebox by diluting an initial stock solution with 1:1 THF/toluene to a final volume of 300 μL with an optical density of 0.3−1.0. All in situ extinction spectra were recorded using a fiber-coupled ASD Inc. PANanalytical spectrometer. To this solution, 50 μL of Brookhart's acid was added to the ICO dispersion, and the extinction spectrum was measured. Following that, 5 μL additions of CoCp$_2^*$ solution were added to the NCs, causing a progressive blue-shift in the LSPR in each measured extinction spectrum. Colloidal stability was initially compromised as indicated by spectral broadening, particularly in smaller NCs, but quickly recovered upon further additions of CoCp$_2^*$. Within 10 additions of CoCp$_2^*$, the LSPR blue-shift had saturated and the titration was complete. This procedure was repeated in triplicate for each ICO NC sample.

HEDA Fittings. The original development of the HEDA model demonstrated for ITO NCs can be found in ref 28. As discussed above, the HEDA model was modified in this work to be more generally applicable to metal oxide NCs. To fit all spectra collected during one titration experiment, the revised HEDA model first intakes the following experimentally measured parameters: extinction spectrum, STEM determined mean and standard deviation in the NC diameter, ICP-OES determined NC volume fraction, the electron effective mass (m_e^*) of the as-synthesized ICO NCs, as calculated from Tauc analysis. The model fits the LSPR according to Drude theory and uses a core−shell geometry to model the plasmonic,

electron-rich core and the surface depletion layer. The fitted extinction spectrum as well as the following fit parameters are output for each spectrum: carrier concentration (n_e), standard deviation in the carrier concentration (σ_{n_e}), bulk mean free path, l_{bulk}, and electron accessible volume fraction, f_e. To account for how m_e^* changes as a function of NC reduction, m_e^* is mathematically represented as a function of n_e (eq S4), in keeping with literature reports for doped CdO.[56]

Furthermore, the HEDA model distinguishes heterogeneous broadening in both the NC diameter and electron concentration by modeling each term as a Gaussian distribution in a probability density function and discretizing these into a 101×101 data point mesh with 10,201 potential combinations. The probability-weighted mesh is used to calculate the complex dielectric function of the plasmonic core, while the depletion layer shell is approximated to have no electron concentration. In fitting the LSPR according to Beer's law and using the measured NC volume fraction, f_e is fit by scaling the volume fractions of the plasmonic core and depleted shell. The HEDA model further deconvolutes contributions from surface scattering and bulk electron scattering in calculating the overall damping. In fitting for l_{bulk}, an upper boundary of 100 nm is placed on the fit to prevent surface scattering from dominating in smaller NCs and infinitely driving up l_{bulk} to compensate. As discussed in more detail in the Supporting Information, we determined that 1/4 was the ideal proportionality factor to describe the size dependence of surface damping in ICO NCs, as opposed to 3/4 for ITO NCs. This proportionality factor was changed to an input parameter in the MATLAB code to make the HEDA model suitable for low-loss plasmonic systems, such as ICO NCs. Further details regarding the HEDA model are located in the Supporting Information, and the MATLAB fitting code can be found at https://github.com/sofiashubert/HEDAfitting.

Ligand Exchange. A 2.0 mg/mL solution of as-synthesized ICO NCs in toluene was precipitated with 0.5 mL of ethanol and centrifuged at 9000 rpm for 10 min. The resulting pellet of ICO NCs was redispersed with a 0.05 M solution of cinnamic acid (0.8 mL)) in their corresponding solvents, for the donating 4H ligand case, chloroform was used, and for the withdrawing 3,5F ligand case, ethyl acetate was used. Right after the pellet is redispersed, the DIPEA base, which had been previously diluted to 0.05 M with chloroform, is added to the solution in a 1:1 volume ratio as the ligand solution, and then, the solution is left for 48 h. Afterward, the ICO NCs in their respective polar solvent were precipitated with hexane and centrifuged at 9000 rpm for 5 min. The pellet of surface-modified ICO NCs was redispersed in their corresponding clean polar solvent again, indicating successful ligand exchange from native oleates to cinnamates.

Superlattice Assembly. ICO NC superlattices were assembled through a slow evaporation process, following the techniques outlined in previous studies.[66,67] A double-side polished and undoped Si substrate (University Wafers) was positioned at a 45° angle in a 4 mL septum sealed vial with 2 mL of ICO NCs in toluene at a concentration of 0.5–2.0 mg/mL. A 20-gauge venting needle was introduced into the septum to regulate the evaporation rate. The vial was then placed in an oven set at 45 °C, remaining undisturbed for approximately 10 days until the complete evaporation of the solvent.

ASSOCIATED CONTENT

ⓈⒾ Supporting Information

The Supporting Information is available free of charge at https://pubs.acs.org/doi/10.1021/acsnano.4c02223.

> Characterization of ICO NC size and doping series, work function analysis from UPS data, experimental replicates of a reducing titration, oxidative titration on reduced ICO NCs, Tauc analysis of ICO NC doping series, effect of the magnitude of A, W_d throughout titration, change in N_e throughout titration, NC reduction dynamics, ICO equilibration experiment,

STEM image of 17% ICO NCs, NMR spectra of as-synthesized and ligand exchanged ICO NCs, valence band maxima region of UPS, W_d for as-synthesized and ligand exchanged ICO NCs, comparison of the spectral shift after NC assembly, GISAXS pattern of 8% ICO NC superlattice, SAXS form factors, HEDA fittings, and comparison of ITO and ICO NC dispersion extinction spectra and superlattice extinction spectra (PDF)

AUTHOR INFORMATION

Corresponding Author

Delia J. Milliron − *Department of Chemistry, University of Texas at Austin, Austin, Texas 78712, United States; McKetta Department of Chemical Engineering, University of Texas at Austin, Austin, Texas 78712, United States;* ⓞ orcid.org/0000-0002-8737-451X; Email: milliron@che.utexas.edu

Authors

Sofia A. Shubert-Zuleta − *Department of Chemistry, University of Texas at Austin, Austin, Texas 78712, United States;* ⓞ orcid.org/0000-0003-0445-175X

Victor Segui Barragan − *Department of Chemistry, University of Texas at Austin, Austin, Texas 78712, United States*

M. Wren Berry − *Department of Chemistry, University of Texas at Austin, Austin, Texas 78712, United States;* ⓞ orcid.org/0000-0003-0260-2585

Robert Russum Jr. − *McKetta Department of Chemical Engineering, University of Texas at Austin, Austin, Texas 78712, United States*

Complete contact information is available at:
https://pubs.acs.org/10.1021/acsnano.4c02223

Notes

The authors declare no competing financial interest.
This work has previously been submitted to a preprint server and can be viewed at ref 76.

REFERENCES

(1) Agrawal, A.; Cho, S. H.; Zandi, O.; Ghosh, S.; Johns, R. W.; Milliron, D. J. Localized Surface Plasmon Resonance in Semiconductor Nanocrystals. *Chem. Rev.* **2018**, *118*, 3121−3207.

(2) Kriegel, I.; Scotognella, F.; Manna, L. Plasmonic Doped Semiconductor Nanocrystals: Properties, Fabrication, Applications and Perspectives. *Phys. Rep.* **2017**, *674*, 1−52.

(3) Comin, A.; Manna, L. New Materials for Tunable Plasmonic Colloidal Nanocrystals. *Chem. Soc. Rev.* **2014**, *43*, 3957−3975.

(4) Luther, J. M.; Jain, P. K.; Ewers, T.; Alivisatos, A. P. Localized Surface Plasmon Resonances Arising From Free Carriers in Doped Quantum Dots. *Nat. Mater.* **2011**, *10*, 361−366.

(5) Wang, K.; Meng, Q.; Wang, Q.; Zhang, W.; Guo, J.; Cao, S.; Elezzabi, A. Y.; Yu, W. W.; Liu, L.; Li, H. Advances in Energy-Efficient Plasmonic Electrochromic Smart Windows Based on Metal Oxide Nanocrystals. *Adv. Energy Sustainability Res.* 2021, 2, 2100117.

(6) Wang, Y.; Runnerstrom, E. L.; Milliron, D. J. Switchable Materials for Smart Windows. *Annu. Rev. Chem. Biomol. Eng.* 2016, 7, 283−304.

(7) Liu, X.; Swihart, M. T. Heavily-doped Colloidal Semiconductor and Metal Oxide nanocrystals: An Emerging New Class of Plasmonic Nanomaterials. *Chem. Soc. Rev.* 2014, 43, 3908−3920.

(8) Bard, A. J.; Bocarsly, A. B.; Fan, F. R. F.; Walton, E. G.; Wrighton, M. S. The Concept of Fermi Level Pinning at Semiconductor/Liquid Junctions. Consequences for Energy Conversion Efficiency and Selection of Useful Solution Redox Couples in Solar Devices. *J. Am. Chem. Soc.* 1980, 102, 3671−3677.

(9) Zum Felde, U.; Haase, M.; Weller, H. Electrochromism of Highly Doped Nanocrystalline SnO2:Sb. *J. Phys. Chem. B* 2000, 104, 9388−9395.

(10) Klein, A.; Albe, K.; Bein, N.; Clemens, O.; Creutz, K. A.; Erhart, P.; Frericks, M.; Ghorbani, E.; Hofmann, J. P.; Huang, B.; et al. The Fermi energy as common parameter to describe charge compensation mechanisms: A path to Fermi level engineering of oxide electroceramics. *J. Electroceram.* 2023, 51, 147−177.

(11) Ephraim, J.; Lanigan, D.; Staller, C.; Milliron, D. J.; Thimsen, E. Transparent Conductive Oxide Nanocrystals Coated with Insulators by Atomic Layer Deposition. *Chem. Mater.* 2016, 28, 5549−5553.

(12) Roman, B. J.; Shubert-Zuleta, S. A.; Shim, G.; Kyveryga, V.; Faris, M.; Milliron, D. J. Facet-Enhanced Dielectric Sensitivity in Plasmonic Metal Oxide Nanocubes. *J. Phys. Chem. C* 2023, 127, 2456−2463.

(13) Zandi, O.; Agrawal, A.; Shearer, A. B.; Reimnitz, L. C.; Dahlman, C. J.; Staller, C. M.; Milliron, D. J. Impacts of Surface Depletion on the Plasmonic Properties of Doped Semiconductor Nanocrystals. *Nat. Mater.* 2018, 17, 710−717.

(14) Tandon, B.; Shubert-Zuleta, S. A.; Milliron, D. J. Investigating the Role of Surface Depletion in Governing Electron-Transfer Events in Colloidal Plasmonic Nanocrystals. *Chem. Mater.* 2022, 34, 777−788.

(15) Brozek, C. K.; Zhou, D.; Liu, H.; Li, X.; Kittilstved, K. R.; Gamelin, D. R. Soluble Supercapacitors: Large and Reversible Charge Storage in Colloidal Iron-Doped ZnO Nanocrystals. *Nano Lett.* 2018, 18, 3297−3302.

(16) Ghini, M.; Curreli, N.; Lodi, M. B.; Petrini, N.; Wang, M.; Prato, M.; Fanti, A.; Manna, L.; Kriegel, I. Control of Electronic Band Profiles Through Depletion Layer Engineering in Core-Shell Nanocrystals. *Nat. Commun.* 2022, 13, 537.

(17) Shubert-Zuleta, S. A.; Tandon, B.; Roman, B. J.; Gan, X. Y.; Milliron, D. J. How to Quantify Electrons in Plasmonic Colloidal Metal Oxide Nanocrystals. *Chem. Mater.* 2023, 35, 3880−3891.

(18) Gibbs, S. L.; Staller, C. M.; Milliron, D. J. Surface Depletion Layers in Plasmonic Metal Oxide Nanocrystals. *Acc. Chem. Res.* 2019, 52, 2516−2524.

(19) Staller, C. M.; Gibbs, S. L.; Saez Cabezas, C. A.; Milliron, D. J. Quantitative Analysis of Extinction Coefficients of Tin-Doped Indium Oxide Nanocrystal Ensembles. *Nano Lett.* 2019, 19, 8149−8154.

(20) Petrini, N.; Ghini, M.; Curreli, N.; Kriegel, I. Optical Modeling of Plasmonic Nanoparticles with Electronically Depleted Layers. *J. Phys. Chem. C* 2023, 127, 1576−1587.

(21) Tandon, B.; Gibbs, S. L.; Dean, C.; Milliron, D. J. Highly Responsive Plasmon Modulation in Dopant-Segregated Nanocrystals. *Nano Lett.* 2023, 23, 908−915.

(22) Tandon, B.; Ghosh, S.; Milliron, D. J. Dopant Selection Strategy for High-Quality Factor Localized Surface Plasmon Resonance from Doped Metal Oxide Nanocrystals. *Chem. Mater.* 2019, 31, 7752−7760.

(23) Agrawal, A.; Kriegel, I.; Runnerstrom, E. L.; Scotognella, F.; Llordes, A.; Milliron, D. J. Rationalizing the Impact of Surface Depletion on Electrochemical Modulation of Plasmon Resonance

Absorption in Metal Oxide Nanocrystals. *ACS Photonics* 2018, 5, 2044−2050.

(24) Conti, C. R., III; McBride, J. R.; Strouse, G. F. Examining the Effect of Dopant Ionic Radius on Plasmonic M:ZnO Nanocrystals (M = Al³⁺, Ga³⁺, In³⁺). *J. Phys. Chem. C* 2021, 125, 7772−7779.

(25) Segui Barragan, V.; Roman, B. J.; Shubert-Zuleta, S. A.; Berry, M. W.; Celio, H.; Milliron, D. J. Dipolar Ligands Tune Plasmonic Properties of Tin-Doped Indium Oxide Nanocrystals. *Nano Lett.* 2023, 23, 7983−7989.

(26) Conti III, C. R.; Quiroz-Delfi, G.; Schwarck, J. S.; Chen, B.; Strouse, G. F. Carrier Density, Effective Mass, and Nuclear Relaxation Pathways in Plasmonic Sn:In₂O₃ Nanocrystals. *J. Phys. Chem. C* 2020, 124, 28220−28229.

(27) Ashcroft, N. W.; Mermin, N. D. *Solid State Physics*; Holt-Saunders, 1976.

(28) Gibbs, S. L.; Staller, C. M.; Agrawal, A.; Johns, R. W.; Saez Cabezas, C. A.; Milliron, D. J. Intrinsic Optical and Electronic Properties From Quantitative Analysis of Plasmonic Semiconductor Nanocrystal Ensemble Optical Extinction. *J. Phys. Chem. C* 2020, 124, 24351−24360.

(29) Araujo, J. J.; Brozek, C. K.; Liu, H.; Merkulova, A.; Li, X.; Gamelin, D. R. Tunable Band-Edge Potentials and Charge Storage in Colloidal Tin-Doped Indium Oxide (ITO) Nanocrystals. *ACS Nano* 2021, 15, 14116−14124.

(30) Schimpf, A. M.; Knowles, K. E.; Carroll, G. M.; Gamelin, D. R. Electronic Doping and Redox-Potential Tuning in Colloidal Semiconductor Nanocrystals. *Acc. Chem. Res.* 2015, 48, 1929−1937.

(31) King, P. D.; Veal, T. D.; Jefferson, P. H.; Zúñiga-Pérez, J.; Muñoz-Sanjosé, V.; McConville, C. F. Unification of the Electrical Behavior of Defects, Impurities, and Surface States in Semiconductors: Virtual Gap States in CdO. *Phys. Rev. B: Condens. Matter Mater. Phys.* 2009, 79, 035203.

(32) Garcia, G.; Buonsanti, R.; Runnerstrom, E. L.; Mendelsberg, R. J.; Llordes, A.; Anders, A.; Richardson, T. J.; Milliron, D. J. Dynamically Modulating the Surface Plasmon Resonance of Doped Semiconductor Nanocrystals. *Nano Lett.* 2011, 11, 4415−4420.

(33) Giannuzzi, R.; De Donato, F.; De Trizio, L.; Monteduro, A. G.; Maruccio, G.; Scarfiello, R.; Qualtieri, A.; Manna, L. Tunable Near-Infrared Localized Surface Plasmon Resonance of F, In-Codoped CdO Nanocrystals. *ACS Appl. Mater. Interfaces* 2019, 11, 39921−39929.

(34) Carroll, G. M.; Brozek, C. K.; Hartstein, K. H.; Tsui, E. Y.; Gamelin, D. R. Potentiometric Measurements of Semiconductor Nanocrystal Redox Potentials. *J. Am. Chem. Soc.* 2016, 138, 4310−4313.

(35) Carroll, G. M.; Schimpf, A. M.; Tsui, E. Y.; Gamelin, D. R. Redox Potentials of Colloidal n-Type ZnO Nanocrystals: Effects of Confinement, Electron Density, and Fermi-Level Pinning by Aldehyde Hydrogenation. *J. Am. Chem. Soc.* 2015, 137, 11163−11169.

(36) Valdez, C. N.; Schimpf, A. M.; Gamelin, D. R.; Mayer, J. M. Proton-Controlled Reduction of ZnO Nanocrystals: Effects of Molecular Reductants, Cations, and Thermodynamic Limitations. *J. Am. Chem. Soc.* 2016, 138, 1377−1385.

(37) Speaks, D. T.; Mayer, M. A.; Yu, K. M.; Mao, S. S.; Haller, E. E.; Walukiewicz, W. Fermi Level Stabilization Energy in Cadmium Oxide. *J. Appl. Phys.* 2010, 107,..

(38) Das, A.; Gautam, S. K.; Shukla, D. K.; Singh, F. Correlations of Charge Neutrality Level with Electronic Structure and p-d Hybridization. *Sci. Rep.* 2017, 7, 40843.

(39) Berry, M. W.; Green, A. M.; Roman, B. J.; Truskett, T. M.; Milliron, D. J. Incorporating Dopant Effects in the Plasmon Ruler for Metal-Oxide Nanocrystal Superlattices. *ACS Mater. Lett.* 2024, 6, 1929−1937.

(40) Liu, Z.; Zhong, Y.; Shafei, I.; Jeong, S.; Wang, L.; Nguyen, H. T.; Sun, C. J.; Li, T.; Chen, J.; Chen, L.; Losovyj, Y.; Gao, X.; Ma, W.; Ye, X. Broadband Tunable Mid-infrared Plasmon Resonances in Cadmium Oxide Nanocrystals Induced by Size-Dependent Nonstoichiometry. *Nano Lett.* 2020, 20, 2821−2828.

(41) Gordon, T. R.; Paik, T.; Klein, D. R.; Naik, G. V.; Caglayan, H.; Boltasseva, A.; Murray, C. B. Shape-Dependent Plasmonic Response and Directed Self-Assembly in a New Semiconductor Building Block, Indium-Doped Cadmium Oxide (ICO). *Nano Lett.* **2013**, *13*, 2857−2863.

(42) Diroll, B. T.; Gordon, T. R.; Gaulding, E. A.; Klein, D. R.; Paik, T.; Yun, H. J.; Goodwin, E. D.; Damodhar, D.; Kagan, C. R.; Murray, C. B. Synthesis of N-type Plasmonic Oxide Nanocrystals and the Optical and Electrical Characterization of Their Transparent Conducting Films. *Chem. Mater.* **2014**, *26*, 4579−4588.

(43) Diroll, B. T.; Guo, P.; Chang, R. P.; Schaller, R. D. Large Transient Optical Modulation of Epsilon-Near-Zero Colloidal Nanocrystals. *ACS Nano* **2016**, *10*, 10099−10105.

(44) Runnerstrom, E. L.; Bergerud, A.; Agrawal, A.; Johns, R. W.; Dahlman, C. J.; Singh, A.; Selbach, S. M.; Milliron, D. J. Defect Engineering in Plasmonic Metal Oxide Nanocrystals. *Nano Lett.* **2016**, *16*, 3390−3398.

(45) Mendelsberg, R.; et al. Determining the Nonparabolicity Factor of the CdO Conduction Band Using Indium Doping and the Drude Theory. *J. Phys. D: Appl. Phys.* **2012**, *45*, 425302.

(46) Kriegel, I.; Urso, C.; Viola, D.; De Trizio, L.; Scotognella, F.; Cerullo, G.; Manna, L. Ultrafast Photodoping and Plasmon Dynamics in Fluorine-Indium Codoped Cadmium Oxide Nanocrystals for All-Optical Signal Manipulation at Optical Communication Wavelengths. *J. Phys. Chem. Lett.* **2016**, *7*, 3873−3881.

(47) Liu, Z.; Beaulac, R. Nature of the Infrared Transition of Colloidal Indium Nitride Nanocrystals: Nonparabolicity Effects on the Plasmonic Behavior of Doped Semiconductor Nanomaterials. *Chem. Mater.* **2017**, *29*, 7507−7514.

(48) Jarzebski, Z. M. Preparation and Physical Properties of Transparent Conducting Oxide Films. *Phys. Status Solidi* **1982**, *71*, 13−41.

(49) Ye, X.; Fei, J.; Diroll, B. T.; Paik, T.; Murray, C. B. Expanding the Spectral Tunability of Plasmonic Resonances in Doped Metal-Oxide Nanocrystals through Cooperative Cation−Anion Codoping. *J. Am. Chem. Soc.* **2014**, *136*, 11680−11686.

(50) Kloper, V.; Osovsky, R.; Kolny-Olesiak, J.; Sashchiuk, A.; Lifshitz, E. The Growth of Colloidal Cadmium Telluride Nanocrystal Quantum Dots in the Presence of Cd^0 Nanoparticles. *J. Phys. Chem. C* **2007**, *111*, 10336−10341.

(51) Ghosh, P. K.; Das, S.; Chattopadhyay, K. K. Temperature Dependent Structural and Optical Properties of Nanocrystalline CdO Thin Films Deposited by Sol-Gel Process. *J. Nanopart. Res.* **2005**, *7*, 219−225.

(52) Lounis, S. D.; Runnerstrom, E. L.; Bergerud, A.; Nordlund, D.; Milliron, D. J. Influence of Dopant Distribution on the Plasmonic Properties of Indium Tin Oxide Nanocrystals. *J. Am. Chem. Soc.* **2014**, *136*, 7110−7116.

(53) Brookhart, M.; Grant, B.; Volpe, A. F., Jr [(3,5-$(CF_3)_2C_6H_3)_4B$]-[$H(OEt_2)_2$]$^+$: A Convenient Reagent for Generation and Stabilization of Cationic, Highly Electrophilic Organometallic Complexes. *Organometallics* **1992**, *11*, 3920−3922.

(54) Graham, A. J.; Gibbs, S. L.; Saez Cabezas, C. A.; Wang, Y.; Green, A. M.; Milliron, D. J.; Keitz, B. K. In Situ Optical Quantification of Extracellular Electron Transfer Using Plasmonic Metal Oxide Nanocrystals. *ChemElectroChem.* **2022**, *9*, 27−49.

(55) Zhu, Y.; Mendelsberg, R. J.; Zhu, J.; Han, J.; Anders, A. Dopant-induced Band Filling and Bandgap Renormalization in CdO:In Films. *J. Phys. D Appl. Phys.* **2013**, *46*, 195102.

(56) Mendelsberg, R. J.; Garcia, G.; Li, H.; Manna, L.; Milliron, D. J. Understanding the Plasmon Resonance in Ensembles of Degenerately Doped Semiconductor Nanocrystals. *J. Phys. Chem. C* **2012**, *116*, 12226−12231.

(57) Gibbs, S. L.; Dean, C.; Saad, J.; Tandon, B.; Staller, C. M.; Agrawal, A.; Milliron, D. J. Dual-Mode Infrared Absorption by Segregating Dopants within Plasmonic Semiconductor Nanocrystals. *Nano Lett.* **2020**, *20*, 7498−7505.

(58) Staller, C. M.; Robinson, Z. L.; Agrawal, A.; Gibbs, S. L.; Greenberg, B. L.; Lounis, S. D.; Kortshagen, U. R.; Milliron, D. J. Tuning Nanocrystal Surface Depletion by Controlling Dopant Distribution as a Route Toward Enhanced Film Conductivity. *Nano Lett.* **2018**, *18*, 2870−2878.

(59) Brown, P. R.; Kim, D.; Lunt, R. R.; Zhao, N.; Bawendi, M. G.; Grossman, J. C.; Bulović, V. Energy Level Modification in Lead Sulfide Quantum Dot Thin Films through Ligand Exchange. *ACS Nano* **2014**, *8*, 5863−5872.

(60) Sato, S.; Kataoka, K.; Jinnouchi, R.; Takahashi, N.; Sekizawa, K.; Kitazumi, K.; Ikenaga, E.; Asahi, R.; Morikawa, T. Band Bending and Dipole Effect at Interface of Metal-Nanoparticles and TiO_2 Directly Observed by Angular-Resolved Hard X-ray Photoemission Spectroscopy. *Phys. Chem. Chem. Phys.* **2018**, *20*, 11342−11346.

(61) Kim, K.; Sherman, Z. M.; Cleri, A.; Chang, W. J.; Maria, J.-P.; Truskett, T. M.; Milliron, D. J. Hierarchically Doped Plasmonic Nanocrystal Metamaterials. *Nano Lett.* **2023**, *23*, 7633−7641.

(62) Jain, P. K.; El-Sayed, M. A. Plasmonic Coupling in Noble Metal Nanostructures. *Chem. Phys. Lett.* **2010**, *487*, 153−164.

(63) Chen, C.-F.; Tzeng, S.-D.; Chen, H.-Y.; Lin, K.-J.; Gwo, S. Tunable Plasmonic Response from Alkanethiolate-stabilized Gold Nanoparticle Superlattices: Evidence of Near-field Coupling. *J. Am. Chem. Soc.* **2008**, *130*, 824−826.

(64) Jain, P. K.; Huang, W.; El-Sayed, M. A. On the Universal Scaling Behavior of the Distance Decay of Plasmon Coupling in Metal Nanoparticle Pairs: A Plasmon Ruler Equation. *Nano Lett.* **2007**, *7*, 2080−2088.

(65) Wang, Y.; Yang, Z.; Wei, J. Surface Plasmon Resonance Properties of Silver Nanocrystal Superlattices Spaced by Polystyrene Ligands. *J. Phys. Chem. C* **2022**, *126*, 4948−4958.

(66) Shevchenko, E. V.; Talapin, D. V.; Murray, C. B.; O'Brien, S. Structural Characterization of Self-Assembled Multifunctional Binary Nanoparticle Superlattices. *J. Am. Chem. Soc.* **2006**, *128*, 3620−3637.

(67) Shevchenko, E. V.; Talapin, D. V.; Kotov, N. A.; O'Brien, S.; Murray, C. B. Structural Diversity in Binary Nanoparticle Superlattices. *Nature* **2006**, *439*, 55−59.

(68) Nordlander, P.; Prodan, E. Plasmon Hybridization in Nanoparticles Near Metallic Surfaces. *Nano Lett.* **2004**, *4*, 2209−2213.

(69) Prodan, E.; Radloff, C.; Halas, N. J.; Nordlander, P. A Hybridization Model for the Plasmon Response of Complex Nanostructures. *Science* **2003**, *302*, 419−422.

(70) Wang, A.; Babcock, J. R.; Edleman, N. L.; Metz, A. W.; Lane, M. A.; Asahi, R.; Dravid, V. P.; Kannewurf, C. R.; Freeman, A. J.; Marks, T. J. Indium-Cadmium-Oxide Films Having Exceptional Electrical Conductivity and Optical Transparency: Clues for Optimizing Transparent Conductors. *Proc. Natl. Acad. Sci. U.S.A.* **2001**, *98*, 7113−7116.

(71) Spencer, J. A.; Mock, A. L.; Jacobs, A. G.; Schubert, M.; Zhang, Y.; Tadjer, M. J. A Review of Band Structure and Material Properties of Transparent Conducting and Semiconducting Oxides: Ga_2O_3, Al_2O_3, In_2O_3, ZnO, SnO_2, CdO, NiO, CuO, and Sc_2O_3. *Appl. Phys. Rev.* **2022**, *9*, 011315.

(72) Staller, C. M.; Gibbs, S. L.; Gan, X. Y.; Bender, J. T.; Jarvis, K.; Ong, G. K.; Milliron, D. J. Contact Conductance Governs Metallicity in Conducting Metal Oxide Nanocrystal Films. *Nano Lett.* **2022**, *22*, 5009−5014.

(73) Greenberg, B. L.; Robinson, Z. L.; Ayino, Y.; Held, J. T.; Peterson, T. A.; Mkhoyan, K. A.; Pribiag, V. S.; Aydil, E. S.; Kortshagen, U. R. Metal-insulator Transition in a Semiconductor Nanocrystal Network. *Sci. Adv.* **2019**, *5*, No. eaaw1462.

(74) Cheref, Y.; Lochon, F.; Daugas, L.; Cleret de Langavant, C.; Larquet, É.; Baron, A.; Gacoin, T.; Kim, J. Dual-band LSPR of Tungsten Bronze Nanocrystals Tunable Over NIR and SWIR Ranges. *Chem. Mater.* **2022**, *34*, 9795−9802.

(75) Jiang, Z. GIXSGUI: A MATLAB Toolbox for Grazing-Incidence X-ray Scattering Data Visualization and Reduction, and Indexing of Buried Three-Dimensional Periodic Nanostructured Films. *J. Appl. Crystallogr.* **2015**, *48*, 917−926.

(76) Shubert-Zuleta, S. A.; Segui Barragan, V.; Berry, M. W.; Russum, R.; Milliron, D. J. How Depletion Layers Govern the

Dynamic Plasmonic Response of In-doped CdO Nanocrystals. *ChemRxiv* **2024**.